Geometry Optimisation of the Muon Production Target for High Energy Physics

Guangyu Xu
Department of Physics, Imperial College London, United Kingdom
(Dated: May 3, 2016)

Intense and coherent muon beams are required for a variety of research programmes in high energy physics. These muons are usually obtained as the decay products of pions produced by bombarding a heavy metal target with a proton beam. In this project, simulations of this muon production system are performed to optimise the target geometry for maximum yields with protons accelerated to 8 GeV. The traditional configuration is based on a cylindrical tungsten target situated inside a superconducting solenoid with a proton beam incident from one end of the solenoid. The backward-scattered pions and muons are captured as the yield of the system. In addition to the optimisation of the dimensions of the cylindrical target, many different geometries are investigated. In particular, a target shaped into a truncated cone is shown to improve the yield up to about 7% compared to the optimum cylindrical target. The other configuration studied is equipped with a proton beam directed onto the target from the side of the solenoid while the pions and muons are collected from both ends of the solenoid. This setup is technically more challenging to implement but provides almost triple yields compared with the traditional configuration.

INTRODUCTION

In the Standard Model of particle physics, the lepton flavour is absolutely conserved due to an exact symmetry. As a result of this stringent conservation law, the neutrino-less decay modes of muons to electrons are forbidden even if the modes are kinematically allowed. For example, the Michel decay mode $\mu^- \rightarrow e^- + \overline{\nu}_e + \nu_\mu$ is an allowed process while the neutrino-less decay $\mu^- \rightarrow e^- + \gamma$ is forbidden within the Standard Model. However, the violation of lepton flavour conservation among neutrino species has been experimentally confirmed with the discovery of neutrino oscillations [1, 2], which urges the Standard Model to be modified. To build a satisfactory theory, a lot of research experiments have been devoted to looking for lepton flavour violation among charged leptons [3], e.g. the neutrino-less decay mode of muons mentioned earlier, and investigating the properties of neutrinos [4], which can be produced in the above Michel decays. Therefore, there is a growing demand for intense muon beams to provide sufficient experimental data for the modification of the Standard Model.

The muon, the second generation lepton, shares a lot of properties with its first generation counterpart, the electron, except that the muon has a much larger mass at 105.9 MeV/c^2 compared with the electron mass of 0.5110 MeV/c^2. Hence, unlike electrons, muons cannot be produced by radioactive decays [5].

The usual method to obtain muons in high energy physics experiments is to accelerate protons and collide them with a fixed target, in which the protons interact with the nucleons inside the target and produce pions via a multitude of channels. The single-pion production threshold is about 280 MeV in the centre-of-mass frame, above which the reaction processes like $p+p \rightarrow p+n+\pi^+$, $p+p \rightarrow p+p+\pi^0$ and $p+n \rightarrow p+p+\pi^-$ become available [6]. At higher energies, further reaction channels open up, allowing the production of multiple pions in a single collision. It is worth noting that although π^0 is produced by these processes in theory, they are not directly detected in the experiments because of their extremely short lifetime at 8.4×10^{-17} s, significantly shorter than the 2.6×10^{-8} s lifetime of $\pi^\pm$ [5]. The charged pions can subsequently decay to muons primarily via $\pi^\pm \rightarrow \mu^\pm + \nu_\mu$ either inside or outside the target, depending on the kinetic energy available for the parent pions.

THEORETICAL BASIS

When a charged particle travels in a matter, there are two principal features charactering its passage [7]. One is the loss of energy due to inelastic collisions with the atomic electrons of the material. The other is the deflection from its incident direction as a result of elastic collisions with the nuclei. Although the reactions occur are by no means restricted to atomic collisions, other processes involved produce negligible effect on the passage in the energy regime interested for this project.

In general, the probability for any interaction of two particles to occur is described in terms of the cross section σ. For a heavy particle with charge z in unit of the elementary charge, a single inelastic collision with atomic electrons is adequately described by the differential cross section [8]

$$\frac{\mathrm{d}\sigma(W;\beta)}{\mathrm{d}W} = \frac{2\pi r_e^2 m_e c^2 z^2}{\beta^2} \frac{(1-\beta^2 W/W_{max})}{W^2} B(W), \quad (1)$$

where W is the energy loss of the particle in a single collision, β is the velocity of the particle in unit of the speed of light, r_e is the classical electron radius, m_e is the electron mass, W_{max} is the maximum energy transfer possible in a single collision and $B(E)$ is a function of E introduced by Bethe [9] to account for the effect of

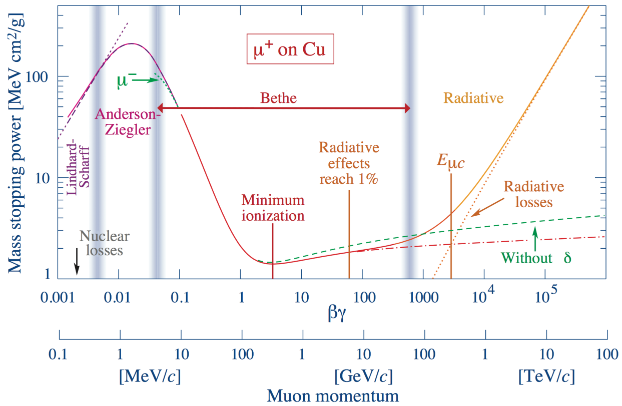

FIG. 1. Stopping power of positive muons in copper as a function of $\beta\gamma = p/Mc$ [8]. The solid curve is the total stopping power and the dotted lines are the approximations valid in specific regimes. The region where the Bethe formula is valid is spanned by the red horizontal arrow.

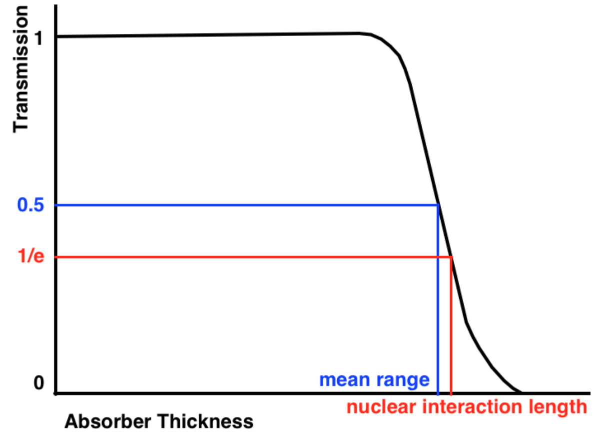

FIG. 2. Typical transmission curve for relativistic charged particles as a function of absorber thickness [7]. The nuclear interaction length is shown in red. The mean range is shown in blue.

the atomic and bulk structure. However, the energy lost in a single collision is generally very small, at typical values less than 100 eV [8]. The particle experiences a large number of collisions before being absorbed by the material. The mean number of collisions with energy loss between W and $W + \mathrm{d}W$ occurring in an infinitesimal distance interval $\mathrm{d}x$ is $n_e \mathrm{d}x\mathrm{d}\sigma$, where n_e is the number density of atomic electrons. Hence the total energy loss through distance $\mathrm{d}x$ is given by

$$\mathrm{d}E = n_e \mathrm{d}x \int_0^{W_{max}} W \frac{\mathrm{d}\sigma(W;\beta)}{\mathrm{d}W} \mathrm{d}W, \tag{2}$$

whereby the stopping power $-\mathrm{d}E/\mathrm{d}x$ is directly obtained as the rate of energy loss of the charged particle along its path in the material [8]. For moderately relativistic charged heavy particles, the stopping power is well described by the Bethe formula in the region $0.1 \lesssim \beta\gamma \lesssim 1000$ with an accuracy of a few percent [8]

$$-\frac{\mathrm{d}E}{\mathrm{d}x} = Kz^2 \frac{Z}{A}\frac{1}{\beta^2}\Big[\frac{1}{2}\ln(L\beta^2\gamma^2 - \beta^2 - \frac{\delta(\beta\gamma)}{2})\Big], \tag{3}$$

where $K = 4\pi N_A r_e^2 m_e c^2$, N_A is the Avogadro constant, $L = 2m_e c^2 W_{max}/I^2$, I is the mean excitation energy, Z and A are the atomic number and atomic mass of the absorber, γ is the relativistic factor and $\delta(\beta\gamma)$ is a correction due to density effect [8]. The computed stopping power of μ^+ in copper is shown in FIG. 1 and the region where the Bethe formula is valid is indicated by the horizontal red arrow.

In practice, it is convenient to know the average penetration range of the particles in a material for a given energy. From a theoretical point of view, this can be calculated by integrating the inverse of the stopping power

$$S(E_0) = \int_0^{E_0} \Big(\frac{\mathrm{d}E}{\mathrm{d}x}\Big)^{-1} \mathrm{d}E, \tag{4}$$

where E_0 is the specified energy of the particles in question [7]. However, the integral only gives an approximate result because the particles are not strictly following a straight path due to the elastic deflections by the nuclei. Therefore, the range is often determined experimentally and a typical relation between the transmission ratio and the absorber thickness is shown in FIG. 2. The nuclear interaction length of a certain material is defined as the distance over which the number of relativistic charged heavy particles is reduced by a factor of $1/e$.

EXPERIMENTAL SETUP

The experiments were simulated via the G4beamline by Muons, Inc. [10], which is a particle tracking programme based on the Monte Carlo code Geat4 [11]. The Bertini cascade physics model was adopted for this project because it reproduces detailed cross section data for nucleons and pions up to 10 GeV [12]. The generated experimental data was then analysed using the ROOT framework developed by CERN [13].

The simulated muon production system consists of a superconducting solenoid, a production target and multiple idealised detectors made of vacuum. In all simulations of this project, the superconducting solenoid was built with 8 m in length and 60 cm in radius, producing a maximum of 5 Telsa magnetic field along its centre line. The energy of the protons in the incident beams was specified to a relatively low level at 8 GeV to suppress the production of anti-protons via the process $p+p \to p+p+p+\overline{p}$ as its cross section increases rapidly at energies above 10 GeV [3]. The target material was selected to be tungsten due to the positive relation between the pion production cross section and the material density [3]. Initially, an idealised pencil beam was used to investigate the effects of altering the target geometry by eliminating any potential effect due to a finite beam width. To obtain more reliable results for practical use, the simulations were repeated for a gaussian beam with a beam radius of 2.5 mm and momentum standard deviation $\Delta p = 64.8$ MeV/c.

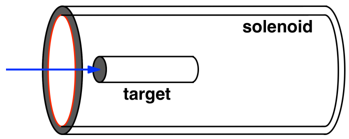

FIG. 3. Traditional configuration with a cylindrical target. The blue arrow represents the incident proton beam. The red circle indicates the upstream detector window where the produced pions and muons are captured. The diagram is not drawn to scale.

The traditional configuration is shown in FIG. 3, which resembles the pion production section of the COMET experiment [3]. The proton beam, indicated by the blue arrow, is incident from one end of the solenoid, parallel to the centre line of the system. Despite of the fact that more pions and muons are produced in the forward direction of the incident beam, the extra yields are mostly undesirable due to their relatively high momenta, which could potentially cause background events [3]. Specifically, the mean momentum of pions collected at the upstream detector is around 200 MeV/c while those at the downstream detector measure a mean momentum of over 700 MeV/c. Hence only the backward-scattered pions and muons are collected at the detector window indicated by the red circle in the diagram.

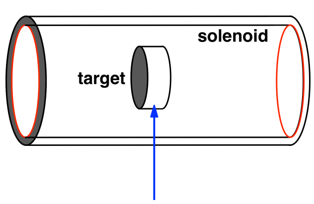

FIG. 4. Side-incident configuration with a cylindrical target. The blue arrow represents the incident proton beam. The red circles indicate both of the detector windows where the produced pions and muons are captured. The diagram is not drawn to scale.

The other configuration is demonstrated in FIG. 4, in which the proton beam is directed onto the target from one side of the solenoid, travelling perpendicular to the centre line of the solenoid. In this case, the pions and muons are captured at both ends because the energetic particles in the forward direction of the incident beam would most likely exit at the opposite side of the solenoid, not contributing to the total yields at the ends.

TRADITIONAL CONFIGURATION

To maximise the yield of the traditional configuration, i.e. the total number of pions and muons collected in the backward direction, a variety of geometries for the tungsten target were tested. In addition, the applicability of a lithium shell wrapping around the tungsten core was investigated.

Cylindrical Target

The simplest geometry in the study is the cylindrical tungsten target already shown in FIG. 3. The initial parameters were obtained from the production target of the COMET experiment [3]. The initial length was set to 160 mm, equivalent to 1.61 times the nuclear interaction length of tungsten [8], and the initial radius was specified at 4 mm. Based on these values, the length and radius of the cylinder were altered independently to find the optimum length at the specified radius, and vice versa. This process was repeated for several times until the change in yield diminished.

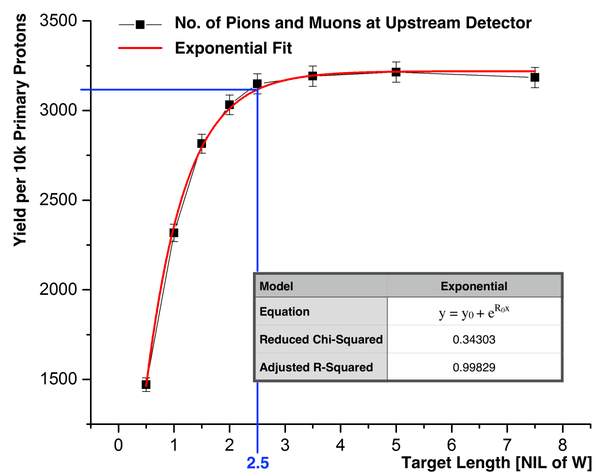

FIG. 5. Yield of backward-scattered pions and muons against target length at a target radius of 2.5 mm for the pencil beam. An exponential function was fitted to the data points as indicated by the red curve.

Shown in FIG. 5 is the plot of the yield against the target length with the pencil beam. The number of pions and muons captured in the upstream detector saturates quickly as the length of the target is increased. The trend is faithfully reproduced by the exponential fit indicated by the red curve. A further increment in length over 2.5 nuclear interaction length does not result in much more interactions as over 90% of the incident protons have already been depleted along the path. Therefore, the target length of 2.5 nuclear interaction length was considered to be the optimum value for this setup.

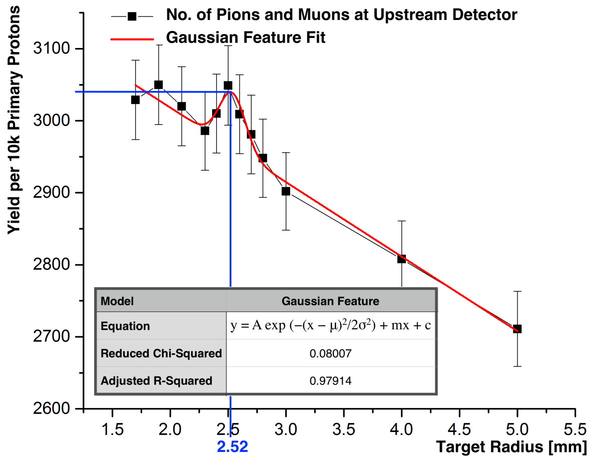

FIG. 6. Yield of backward-scattered pions and muons against target radius at a target length of 2.5 nuclear interaction length for the pencil beam. A gaussian feature was fitted on top of a linear function for the data points as indicated by the red curve.

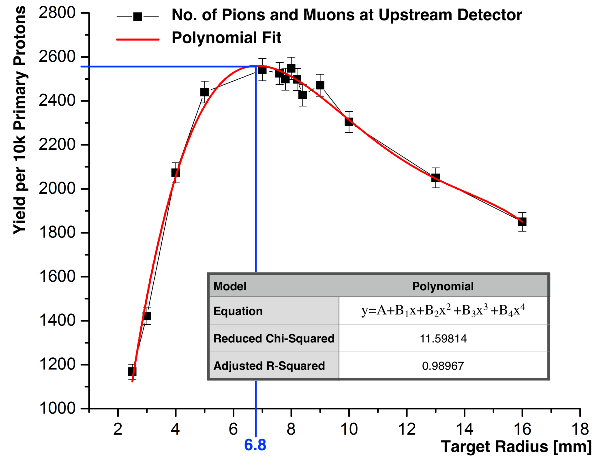

FIG. 7. Yield of backward-scattered pions and muons against target radius at a target length of 2.5 nuclear interaction length for the gaussian beam of 2.5 mm radius. A fourth order polynomial was fitted to the data points as indicated by the red curve.

The plot of the yield against the target radius for the pencil beam is shown in FIG. 6. The yield of pions and muons almost drops linearly with the increase of target radius because the additional material in the radial direction significantly increases the path length of pions and hinder their escape from the target. In the plot, a small gaussian feature superposed on a linear function was fitted to the obtained results, indicating a peak value at a radius of 2.52 mm. However, at smaller radii, the trend is not immediately evident and the fluctuations are most likely to be just statistical noise, which are of comparable size to the uncertainties attached to these data points. Although the fitted curve shows a good agreement with this particular set of measurements, the gaussian feature is likely to be a coincidence rather than a consequence of the physics behind. The yields at radii between 1.75 mm and 2.75 mm are virtually equivalent considering the large uncertainties in the measurements. In the end, the value of 2.52 mm was still accepted as the optimum radius because it is one of those equivalently good choices, which is also not too small if a finite beam width is taken into account in practice.

For the gaussian beam of 2.5 mm radius, the saturation of the yield at larger target length follows exactly the same pattern as for the pencil beam. The optimum length was again chosen to be 2.5 nuclear interaction length. At this target length, the variation of yield for different target radii is shown in FIG. 7, which exhibits a completely different pattern from the previous case of the pencil beam. The general shape of these data points is represented by the fitted fourth order polynomial drawn in red, which peaks at a target radius of 6.8 mm. In the direction of increasing target radius, the rise in the yield at small radii is due to the fact that more protons in the gaussian beam could actually collide with the target and interact with the nucleons to produce pions. However, this effect is gradually outweighed by the suppression in the yield because of the additional material trapping more pions inside, resulting in an overall decline in the total yield after the maximum. The optimum radius of the target for the gaussian beam was readily decided to be 6.8 mm corresponding to the maximum yield. However, as expected for introducing a finite beam width, this time the maximum yield is about 20% less than the value for the case of the pencil beam.

Truncated Conical Target

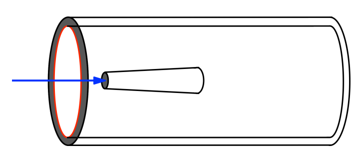

FIG. 8. Traditional configuration with a target of truncated cone. The diagram is not drawn to scale.

Another geometry investigated for the tungsten target in the traditional setup is a truncated cone shown in FIG. 8. The motivation for a conical target is that although the system should be rotationally symmetric about the centre line of the solenoid, there is no requirement for the target to be uniform alone the centre line by symmetry considerations. In addition, a smaller front radius might be able to facilitate the escape of pions in the backward direction and suppress the yield in the forward direction. To make direct comparison with the previous results for each of the two beam types, the initial

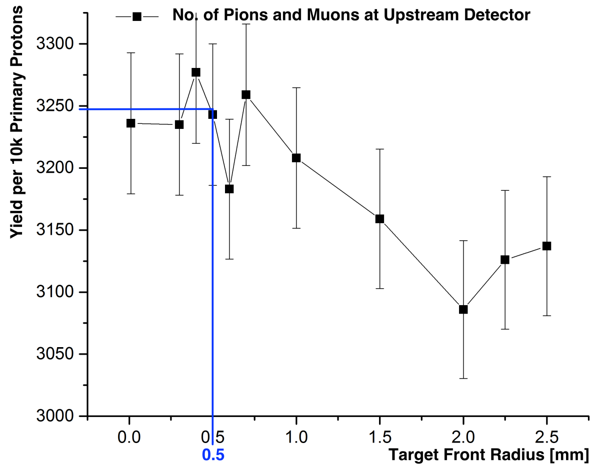

FIG. 9. Yield of backward-scattered pions and muons against target front radius at a target length of 2.5 nuclear interaction length for the pencil beam.

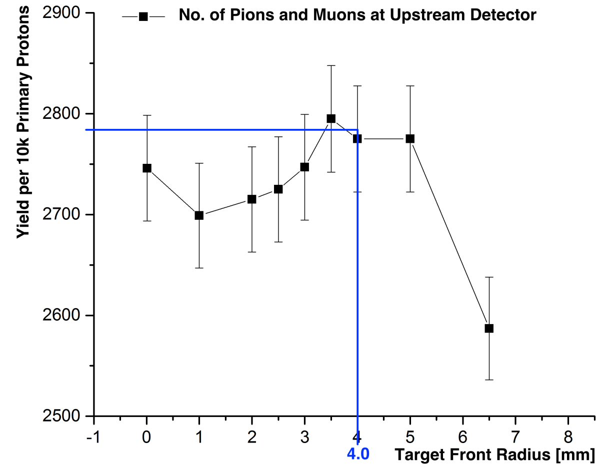

FIG. 10. Yield of backward-scattered pions and muons against target front radius at a target length of 2.5 nuclear interaction length for the gaussian beam of 2.5 mm radius.

dimensions of the truncated cone were set to be identical to the corresponding cylindrical target optimised in the previous section. The target length and the amount of material used to forge the target were kept constant while the two radii were adjusted to examine the change in the yield.

Shown in FIG. 9 and FIG. 10 are the plots of the yield against the front radius of the truncated cone for the two distinct beam types. As the front radius of the target increases from 0 to 2.5 mm or 6.8 mm depending on the beam type, the target transforms from a simple cone to a truncated cone, eventually reduces to a cylinder. The scale of variations in the yield are much smaller in these plots. Hence the relatively large uncertainties make a functional fit impractical. However, despite of these large errors, the general trends in FIG. 9 and FIG. 10 still respectively resemble those of FIG. 6 and FIG. 7 in a crude snese. In the case of the pencil beam shown in FIG. 9, the yield still falls as the front radius increases. The abrupt turning point at 2.0 mm front radius is most likely to be due to statistical errors rather than the physical properties of the system. The points between 0 and 1.0 mm in the plot are equally adequate choices for the optimum value of the front radius, therefore the mean value of 0.5 mm was chosen to be the representative. For the gaussian beam, FIG. 10 shows a growth in yield from about 1.0 mm front radius until the maximum at roughly 4.0 mm is reached. Then the yield declines as the target reduces to the simple cylinder. The anomaly point at 0 can be safely neglected considering the large uncertainty. Similar to the arguments above, the optimum front radius for the gaussian beam was determined to be 4.0 mm.

Complicated But Ineffective Geometries

Besides the two simple geometries discussed above, there were a lot of more complicated trials for the traditional configuration but all failed to improve over the simple ones. Presented in this section are a few of those ineffective examples investigated for this project.

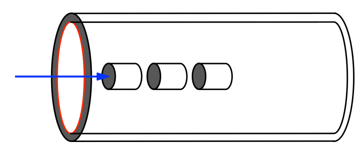

FIG. 11. Traditional configuration with a cylindrical target of sliced structure. The diagram is not drawn to scale.

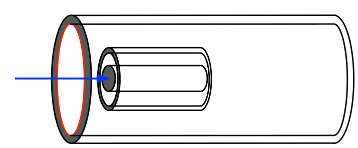

FIG. 12. Traditional configuration with a cylindrical target of layered structure. The diagram is not drawn to scale.

The incentive for using the sliced or the layered structures shown in FIG. 11 and FIG. 12 is to allow more pions to escape the target while retaining a relatively long path length for the protons to further interact. Although a wide range of parameters for these geometries were tested in the simulations, they either delivered no improvement at all or a reduction of yields in all directions were observed.

The deployment of a lithium shell around the tungsten core illustrated in FIG. 13 was considered to be the most promising arrangement for the traditional configuration.

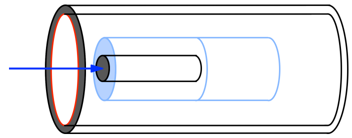

FIG. 13. Traditional configuration with a target consisted of tungsten core and a lithium shell. The lithium part is shown in light blue surrounding the black tungsten core. The diagram is not drawn to scale.

The primary objective of introducing a supplementary lithium wrapping is to slow down the energetic pions produced in the tungsten core and foster their decays to muons, therefore reducing the mean momenta of the captured pions and muons. From a practical perspective, the liquid lithium could also be circulated to serve as the coolant for the hot tungsten core instead of using water cooling. Unfortunately, according to the simulation data obtained in this project, the addition of lithium failed to reduce the momenta of pions and muons, and simultaneously led to a significant reduction in the yield across the entire momentum spectrum.

SIDE-INCIDENT CONFIGURATION

For the traditional configuration discussed in the previous section, only the backward-scattered pions and muons were recognised as the yield of the system because of the contamination of high energy pions and muons in the forward direction. Consequently, even those pions and muons emitted in the forward direction with a desirable energy level were wasted in the the traditional setup. Therefore, a configuration with the proton beam incident from the side of the solenoid was proposed to resolve this problem as already illustrated in FIG. 4. In this scenario, those highly energetic pions and muons produced in the forward direction of the proton beam are extracted from the opposite side of the solenoid, without contaminating the low energy pions and muons collected at either end of the solenoid. Compared with the traditional configuration, the pions obtained in this side-incident setup only carry about 40% more momentum on average while the mean momentum of muons collected is merely 10% higher, which was regarded as a necessary compromise for almost tripling the yield of the system. For simplicity, a thin cylindrical tungsten plate of large radius was deployed as the production target in this configuration. Since the magnetic field produced by the solenoid is perpendicular to the incident direction of the proton beam, the Lorentz force bends the path of the protons to a small extent. To compensate for this effect and maximise the path length of protons inside the target, a slight offset for the position of proton source was made in the opposite direction of the bending.

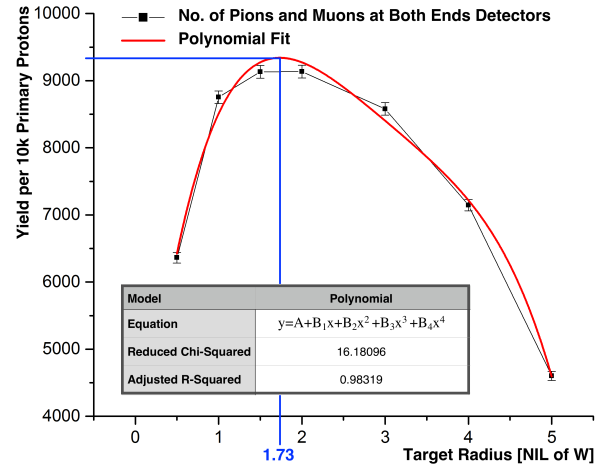

FIG. 14. Yield of pions and muons at both ends of the solenoid against target radius at a target thickness of 3.0 mm for the pencil beam. A fourth order polynomial was fitted to the data points as indicated by the red curve.

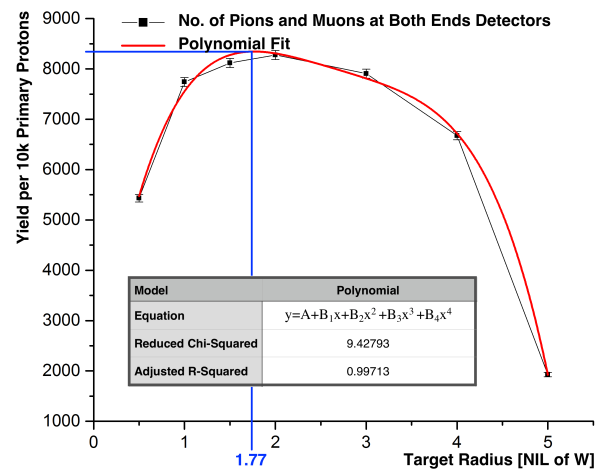

FIG. 15. Yield of pions and muons at both ends of the solenoid against target radius at a target thickness of 11.0 mm for the gaussian beam of 2.5 mm radius. A fourth order polynomial was fitted to the data points as indicated by the red curve.

Shown in FIG. 14 and FIG. 15 are the plots of the yield of muons and pions captured at both ends of the solenoid against the radius of the target for the two beam types. Since the proton beam is directed from the side and travels across the diameter of the target, the target radius here plays a similar role as the target length discussed in the traditional configuration. However, unlike the distinct feature of yield saturation found in FIG. 5, the yields in the side-incident configuration culminate at an optimum target radius of about 1.75 nuclear interaction length for both beam types, which are approximately represented by the fourth order polynomials fitted into the plots. With increasing radius, the boost in yields at smaller radii is obviously due to the extended path length for the protons. But as the radius is increased beyond

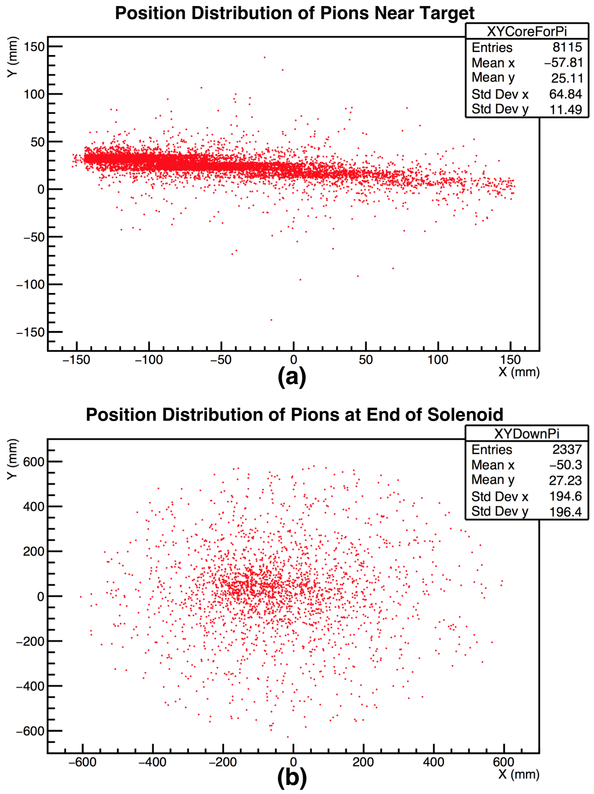

FIG. 16. Position distribution of pions produced by the target of optimum radius (a) immediately at one end of the target (b) at one end of the solenoid.

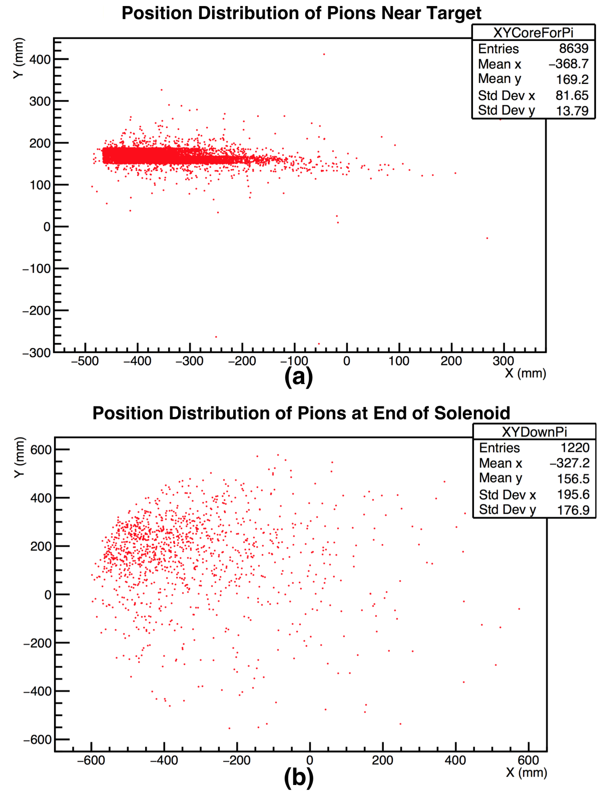

FIG. 17. position distribution of pions produced by the target of large radius (a) immediately at one end of the target (b) at one end of the solenoid.

the optimum value, more protons are exhausted in the interactions near the wall of the solenoid and the position distributions of the pions released from the ends of the target are shifted towards the edge from FIG. 16 to FIG. 17. Consequently, the number of pions and muons that are able to make their way to the ends of the solenoid is gradually reduced at larger target radius because those near the wall of the solenoid are prone to the absorption by the solenoid during the flight.

The changes in the yield due to variations in the target thickness for the pencil beam and the gaussian beam are respectively drawn in Fig. 18 and FIG. 19. As the thickness of this target is in the direction along which the pions and muons are most likely to escape, it should be considered to be an equivalent quantity to the target radius studied for the cylindrical target in the traditional configuration. However, the plots here for both beam types demonstrate a similar shape with the plot of yield against the target radius for the gaussian beam shown in FIG. 7. The lack of analogy between FIG. 18 and FIG. 6 for the pencil beam is not immediately apparent but might be due to the fact that at small radii the actual path length of the protons inside the target is more sensitive to the target thickness of the cylindrical plate in the side-incident configuration than to the target radius of the cylinder implemented in the traditional configuration. In the traditional setup, even if a proton escapes the target in the radial direction, the Lorentz force would guide it to return into the target, which means a smaller radius would not reduce the path length of the protons significantly. In contrast, for the side-incident configuration, a small deviation of the proton path in the direction of the centre line of the solenoid would lead to an inevitable escape of that proton, which could not be retrieved by the Lorentz force imposed by the parallel magnetic field. So the actual path length in this case would be shortened significant for small values of the target thickness. Nevertheless, from a phenomenological perspective, the maximum yields indeed occur at target thickness values of 3.0 mm for the pencil beam and 11.4 mm for the gaussian beam, which were deemed as the corresponding optimum values in this configuration.

SIMULATION RESULTS

With all the optimum values obtained for the parameters of the production target, the simulations for each of the geometries discussed above were performed with both the pencil beam and the gaussian beam, consuming 1.0×10^5 incident protons in each run. The obtained results of yields as well as the plots for the total momentum

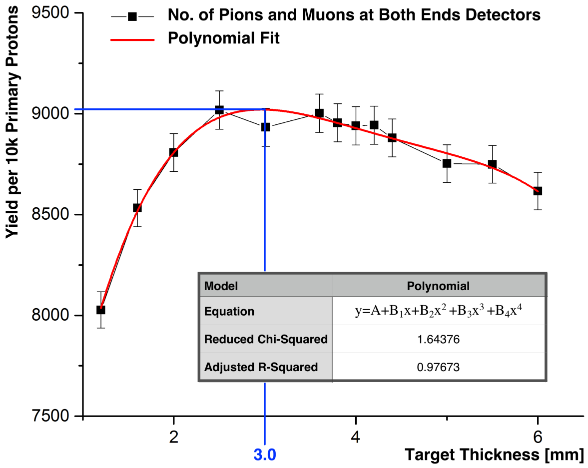

FIG. 18. Yield of pions and muons at both ends of the solenoid against target thickness at a target radius of 1.75 nuclear interaction length for the pencil beam. A fourth order polynomial was fitted to the data points as indicated by the red curve.

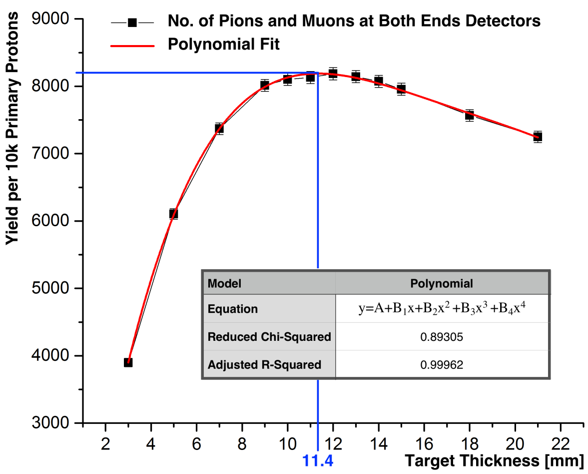

FIG. 19. Yield of pions and muons at both ends of the solenoid against target thickness at a target radius of 1.75 nuclear interaction length for the gaussian beam of 2.5 mm radius. A fourth order polynomial was fitted to the data points as indicated by the red curve.

distributions are shown below in this section.

The yields in the case of the pencil beam are summarised in TABLE I. For the traditional configuration, the optimised cylindrical target of 2.52 mm radius and 249 mm length provides 15% more pions and muons compared with the original COMET target of 4.00 mm radius and 160 mm length. The adoption of the truncated cone delivers a further improvement of approximately 7% in the combined yield. In contrast, the side-incident configuration with the cylindrical plate provides significantly higher yields, almost tripling the numbers achieved in the traditional configuration. As for the gaussian beam of 2.5 mm radius with $\Delta p = 64.8$ MeV/c, the figures in

Geometry	No. of Pions	No. of Muons	Combined Yield
	Traditional Configuration		
COMET	13183	13088	26271
Cylinder	15350	14998	30348
Cone	16140	15941	32081
	Side-Incident Configuration		
Plate	44201	45490	89691

TABLE I. Yields of pions and muons for the pencil beam of 1.0×10^5 protons.

Geometry	No. of Pions	No. of Muons	Combined Yield
	Traditional Configuration		
Cylinder	13231	12143	25374
Cone	14130	13008	27138
	Side-Incident Configuration		
Plate	44465	39053	83518

TABLE II. Yields of pions and muons for the gaussian beam of 1.0×10^5 protons.

TABLE II show a similar pattern as those for the pencil beam in TABLE I, although each of them is consistently less than their corresponding entry found for the pencil beam, as an expected effect due to the finite beam width.

The total momentum distributions of the pions and muons produced with the pencil beam for the traditional and the side-incident configurations are shown in FIG. 20 and FIG. 21 respectively. The corresponding plots for the gaussian beam are not included as they share exactly the same features besides their relatively low peaks. In FIG. 20 for the traditional configuration, the results for the COMET target, the optimised cylinder and the truncated cone are respectively colour-coded in black, blue and red. The blue and red curves in FIG. 21 of the side-incident configuration represent the pions or muons collected at each of the two ends of the solenoid. Comparing the diagrams for the two distinct configurations, the most probably momentum of the collected pions, i.e. the peak value, are found to be identical at about 160 MeV/c for both configurations but there are considerably more pions in the 200 – 400 MeV/c range for the side-incident case. Regarding to the momentum distributions of muons, there shows a primary peak at about 100 MeV/c as well as a small but abrupt secondary peak at approximately 230 MeV/c in both configurations, although the distribution for the side-incident case exhibits a longer tail beyond 400 MeV/c. The energy at the secondary peaks, i.e. 230 MeV is in fact around the minimum ionisation energy of muons in tungsten [8]. The muons at this energy level experience the least ionisation when travelling inside tungsten, which means they are the ones that are most likely to escape the target. Therefore, the secondary peaks found in the momentum

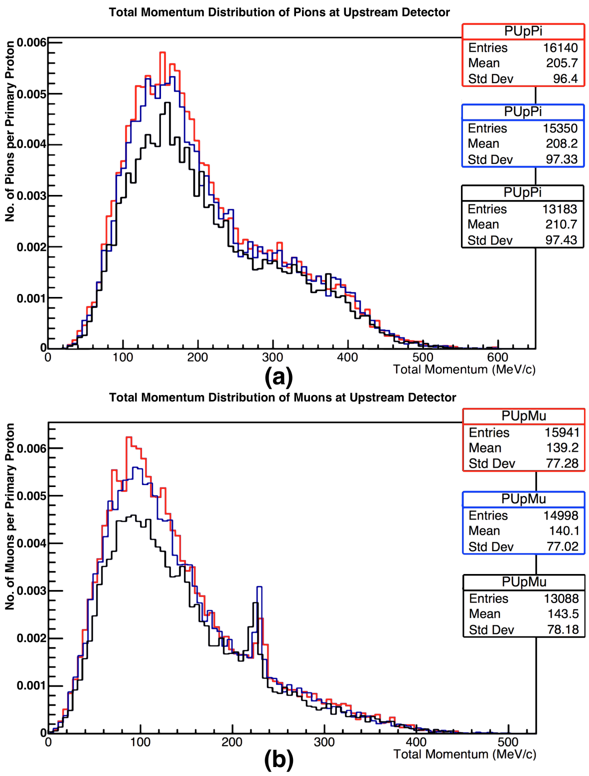

FIG. 20. Momentum distribution of (a) pions and (b) muons at upstream detector in the traditional configuration with the pencil beam. The black, blue and red curves are respectively for the COMET target, the optimised cylindrical target and the truncated conical target.

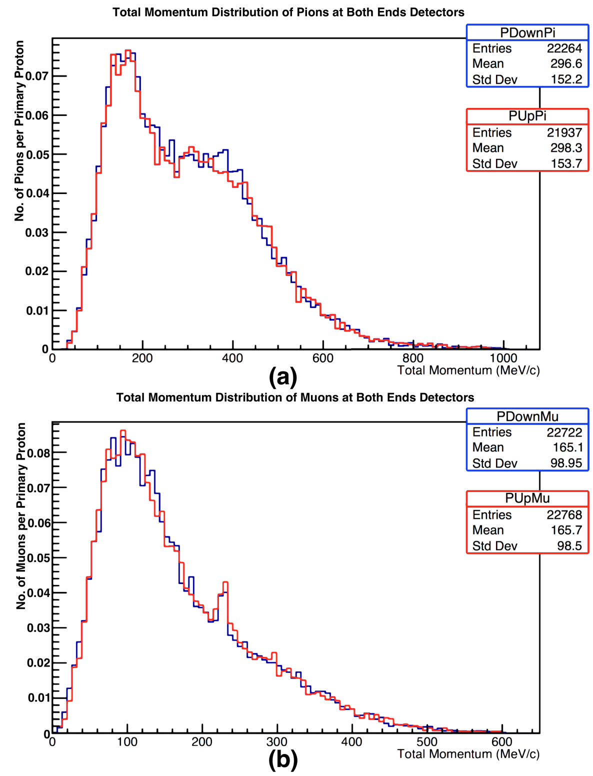

FIG. 21. Momentum distribution of (a) pions and (b) muons for both detectors at the ends of the solenoid in the side-incident configuration with the pencil beam. The blue and red curves correspond the two independent detectors.

distributions of muons are at least partially contributed by these minimum ionising muons produced inside the production target, although their exact origin is not fully understood.

CONCLUSION

During the study of this project, a variety of geometries had been investigated in the simulated muon production system in order to maximise the combined yield of relatively low energy pions and muons. With the proton beam accelerated to 8 GeV, the Bertini cascade model in the Geat4 package was implemented to predict the yields delivered by different tungsten targets arranged in two distinctive configurations. A straight superconducting solenoid generating a 5 Tesla magnetic field at its centre line was used to confine the charged particles.

For the traditional configuration in which the proton was incident from one end of the solenoid, the target forged into a truncated cone was proven to produce up to 7 % more yield in the backward direction than its cylindrical counterpart of identical mass and length. In the configuration where the proton beam was directed onto the target from the side of the solenoid, a thin cylindrical plate made of tungsten was demonstrated to deliver almost triple yield compared with the traditional configuration, at the expense of slightly raising the mean momentum of the collected pions and muons. In practice, while the truncated conical target could be easily implemented in real experiments, the applicability of the side-incident configuration would be difficult to justify in the scope of this project alone. The potential problems include the risk of damaging the solenoid due to the energetic particles produced in the forward direction of the incident proton beam. Moreover, extracting pions and muons at both ends of the solenoid would double the cost of the transport line and the increased mean momentum would escalate the requirements for the muon cooling system as well.

ACKNOWLEDGEMENTS

This project is a co-operative effort with Shaoyan Zang. The patient guidance and advice from Dr. Ajit Kurup and Dr. Jaroslaw Pasternak are gratefully acknowledged.

[1] Y. Fukuda, T. Hayakawa, *et al.* (Super-Kamiokande Collaboration), Phys. Rev. Lett. **81**, 1562 (1998).

[2] S. Fukuda, Y. Fukuda, *et al.* (Super-Kamiokande Collaboration), Phys. Rev. Lett. **86**, 5656 (2001).

[3] Y. Kuno *et al.* (COMET Collaboration), J-PARC PAC E **21** (2012).

[4] S. Choubey *et al.* (IDS-NF), (2011), arXiv:1112.2853.

[5] I. S. Hughes, *Elementary Particles*, 3rd ed. (Cambridge University Press, 1991).

[6] F. Berg *et al.*, Phys. Rev. Accel. Beams **19**, 024701 (2016), arXiv:1511.01288 [physics.ins-det].

[7] W. R. Leo, *Techniques for nuclear and particle physics experiments: a how-to approach* (Springer Science & Business Media, 2012).

[8] K. A. Olive *et al.* (Particle Data Group), Chin. Phys. **C38**, 090001 (2014).

[9] H. Bethe, Annalen der Physik **397**, 325 (1930).

[10] T. Roberts, *G4beamline Users Guide* (2012).

[11] M. Ellis *et al.*, in *Astroparticle, Particle and Space Physics, Detectors and Medical Physics Applications: Proceedings of the 9th Conference: Villa Olmo, Como, Italy, 17-21 October 2005* (World Scientific, 2006) p. 462.

[12] *Geat4 Physics Reference Manual* (2015).

[13] *Root User Guide* (2014).